Graphene and Relativistic Quantum Physics

Philip Kim
Department of Physics
Columbia University New York
New York 10027, USA

1 Introduction

Graphene is one atom thick layer of carbon atoms arranged in a honeycomb lattice. This unique 2-dimensional (2D) crystal structures provide an additional degree of freedom, termed as pseudo spin, to describe the orbital wave functions sitting in two different sublattices of the honeycomb lattice. In the low energy spectrum of graphene near the charge neutrality point, where the linear carrier dispersion mimics the "quasi-relativistic" dispersion relation, pseudo spin replaces the role of real spin in the usual relativistic Fermion energy spectrum. The exotic quantum transport behavior discovered in graphene, such as the unusual half-integer quantum Hall effect and Klein tunneling effect, are a direct consequence of this analogical "quasi relativistic" quantum physics. In this lecture, I will make a connection of physics in graphene to relativistic quantum physics employing the concept of pseudo-spin.

Many of the interesting physical phenomena appearing in graphene are governed by the unique chiral nature of the charge carriers in graphene owing to their quasi relativistic quasiparticle dynamics described by the effective massless Dirac equation. This interesting theoretical description can be dated back to Wallace's early work of the electronic band structure calculation of graphite in 1947 where he used the simplest tight binding model and correctly captured the essence of the electronic band structure of graphene, the basic constituent of graphite [1]. Fig. 1 shows the reconstructed the band structure of electrons in graphene where the energy can be expressed by 2D momentum in the plane. The valence band (lower band) and conduction band (upper band) touch at six points, where the Fermi level is located. In the vicinity of these points, the energy dispersion relation is linear, mimicking massless particle spectrum in relativistic physics. As we will later discuss in detail, this interesting electronic structures also exhibit the chiral nature of carrier dynamics, another important characteristics of relativistic quantum particles, rediscovered several times in graphene in different contexts [2, 3, 4, 5].
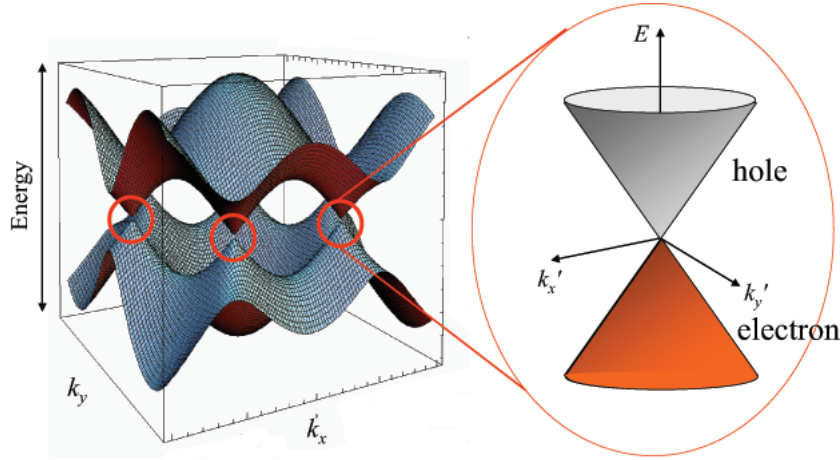
Figure 1: Energy band structure of graphene. Linear dispersion relation near the central part of the bands are highlighted. Reproduced from Ref.[10].

In the following sections, after a brief survey of early experiments related to graphene, we will focus on the chiral nature of the electron dynamics in mono-layer graphene where the electron wave function's pseudo-spin plays an important role. We will present two experimental examples: the half-integer QHE [6, 7] and the Klein tunneling effect in graphene [8]. The quasi relativistic quantum dynamics of graphene has provided a compact and precise description for these unique experimental observations and further providing a playground for implementing tests of quantum electrodynamics (QED) in a simple experimental situation [9], where electron Fabry-Perrot oscillations were recently observed [8].

2   Early Experiment

Independent to earlier theoretical works, experimental efforts to obtain graphene dated back to Böhm *et al.*'s early work of transmission electron microscopy [11] and the early chemical deposition growth of graphene on metal surfaces developed in the 1990s [12]. In the past decade, renewed efforts to obtain the atomically thin graphite have been pursued through several different routes. In retrospect, these various methods fall into two categories: the bottom-up approach and the top-down approach. In the former, one started with carbon atoms and one tries to assemble graphene sheets by chemical pathways [13, 14]. This is best exemplified by work of the W. A. de Heer group at the Georgia Institute of Technology. In Ref. [14], they demonstrated that thin graphite films can be grown by thermal decomposition on the (0001) surface of 6H-SiC. This method opens the way to large scale integration of nanoelectronics based on graphene. Recent progress through this chemical approach to graphene synthesis has had dazzling successes by diverse routes, including epitaxial graphene growth [15], chemical vapor deposition [16, 17], and solution processing [18].

On the other hand, the top-down approach starts with bulk graphite, which essentially involves graphene sheets stacked together, and tries to extract graphene sheets from the bulk by mechanical exfoliation. The mechanical extraction of layered material dates back to the 1970s. In his seminal experiment [19], Frindt showed that few layers of superconducting $NbSe_2$ can be mechanically cleaved from a bulk

crystal fixed on an insulating surface using epoxy. While it is known for decades that people routinely cleave graphite using scotch tape when preparing sample surfaces for Scanning Tunneling Microscopy (STM) study and all optics related studies, the first experiment explicitly involving the mechanical cleavage of graphite using scotch tape was carried out by Ohashi *et al.* [20]. The thinnest graphite film obtained in this experiment was about 10 nm, corresponding to ~30 layers.

Experimental work to synthesize very thin graphitic layers directly on top of a substrate [21] or to extract graphene layers using chemical [22] or mechanical [23, 24, 25] exfoliation was demonstrated to produce graphitic samples with thicknesses ranging from 1 to 100 nm. Systematic transport measurements have been carried out on mesoscopic graphitic disks [26] and cleaved bulk crystals [20] with sample thicknesses approaching ~20 nm, exhibiting mostly bulk graphite properties at these length scales. More controllability was attempted when Ruoff *et al.* worked out a patterning method for bulk graphite into a mesoscopic scale structure to cleave off thin graphite crystallites using atomic force microscopy [25].

A sudden burst of experimental and theoretical work on graphene followed the first demonstration of single- and multi-layered graphene samples made by a simple mechanical extraction method [27], while several other groups were trying various different routes concurrently [28, 29, 14]. The method that Novoselov et al. used was pretty general, and soon after, it was demonstrated to be applicable to other layered materials [30]. This simple extraction technique is now known as the mechanical exfoliation method. It also has a nick name, "scotch tape" method, since the experimental procedure employs adhesive tapes to cleave off the host crystals before the thin mesocoscopic samples are transferred to a target substrate, often a silicon wafer coated with a thin oxide layer. A carefully tuned oxide thickness is the key to identify single layer graphene samples among the debris of cleaved and transferred mesoscopic graphite samples using the enhanced optical contrast effect due to Fabry-Perot interference [31].

Since this first demonstration of experimental production of an isolated single atomic layer of graphene sample, numerous unique electrical, chemical, and mechanical properties of graphene have been investigated. In particular, an unusual half-integer quantum Hall effect (QHE) and a non-zero Berry's phase [6, 7] were discovered in graphene, providing unambiguous evidence for the existence of Dirac fermions in graphene and distinguishing graphene from conventional 2D electronic systems with a finite carrier mass.

3 Pseudospin Chirality in Graphene

Carbon atoms in graphene are arranged in a honeycomb lattice. This hexagonal arrangement of carbon atoms can be decomposed into two interpenetrating triangular sublattices related to each other by inversion symmetry. Taking two atomic orbitals on each sublattice site as a basis (See Fig. 2), the tight binding Hamiltonian can be simplified near two inequivalent Brillouin zone corners, $\mathbf{K}$ and $\mathbf{K}'$) as

$$\hat{H} = \pm \hbar v_F \boldsymbol{\sigma} \cdot (-i\hbar \boldsymbol{\nabla}), \tag{1}$$

where $\boldsymbol{\sigma} = (\sigma_x, \sigma_y)$ are the Pauli matrices , $v_F \approx 10^6$ m/s is the Fermi velocity in graphene and the $+$ $(-)$ sign corresponds to taking the approximation that the wave vector $\mathbf{k}$ is near the $\mathbf{K}$ $(\mathbf{K}')$ point.
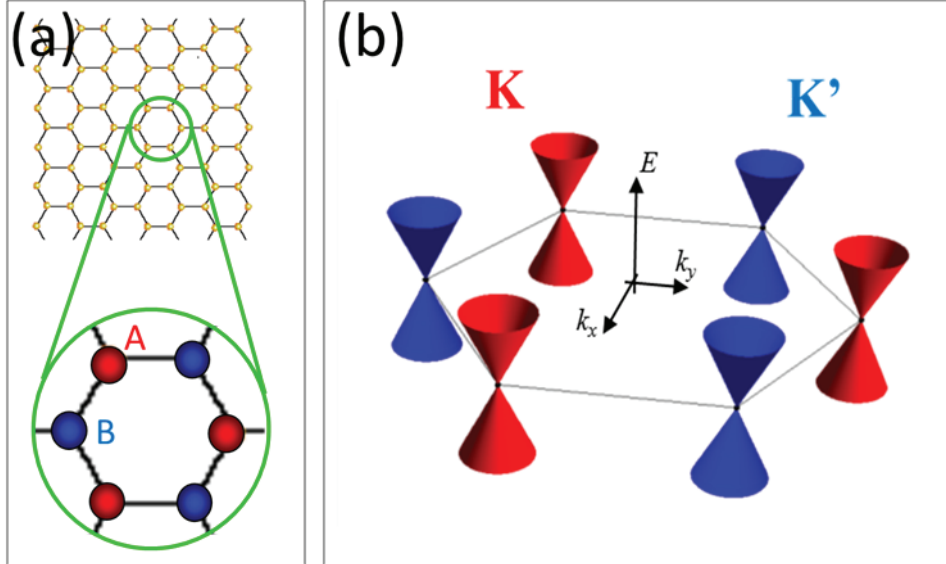
Figure 2: (a) Real space image of graphene lattice structure. Two different sub-lattices are marked by red and blue color. (b) Low energy approximation of energy band near the charge neutrality of graphene energy band. Two inequivalent corner of the Brillouin zone are marked by **K** and **K'**, respectively.

The structure of this "Dirac" equation is interesting for several reasons. First, the resulting energy dispersion near the zone corners is linear in momentum, $E(\kappa) = \pm \hbar v_F |\kappa|$, where the wave vector κ is defined relative to **K**(or **K'**), i.e., $\boldsymbol{\kappa} = \mathbf{k} - \mathbf{K}$(or **K'**). Consequently, the electrons near these two Dirac points always move at a constant speed, given by the Fermi velocity $v_F \approx c/300$ (rather than the real speed of light c). The electron dynamics in graphene are thus effectively "relativistic", where the speed of light is substituted by the electron Fermi velocity v_F. In a perfect graphene crystal, the Dirac points (**K** and **K'**) are coincident with the overall charge neutrality point (CNP), since there are two carbon atoms in the unit cell of graphene and each carbon atom contributes one electron to the two bands, resulting in the Fermi energy E_F of neutral graphene lying precisely at the half-filled band.

For the Bloch wave function near **K'**, the "Dirac" equation in Eq. (1) can be rewritten as

$$\hat{H} = \pm \hbar v_F \boldsymbol{\sigma} \cdot \boldsymbol{\kappa} . \tag{2}$$

The solution of this massless Dirac fermion Hamiltonian is studied by [32, 5, 33]:

$$|\boldsymbol{\kappa}\rangle = \frac{1}{\sqrt{2}} e^{i\boldsymbol{\kappa}\cdot\mathbf{r}} \begin{pmatrix} -ise^{-i\theta_\kappa/2} \\ e^{i\theta_\kappa/2} \end{pmatrix} , \tag{3}$$

where θ_κ is the angle between $\boldsymbol{\kappa} = (\kappa_x, \kappa_y)$ and the y-axis, and $s = +1$ and -1 denote the states above and below **K**, respectively. The corresponding energy for these states is given by

$$E_s(\kappa) = s\hbar v_F |\boldsymbol{\kappa}|, \tag{4}$$

where $s = +1/-1$ is an index for the positive/negative energy band, respectively. The two components of the state vector give the amplitudes of the electronic wave

functions on the atoms of the two sublattices, so the angle θ_κ determines the character of the underlying atomic orbital mixing.

The two-component vector in formula in Eq. (3) can be viewed as a result of a spinor-rotation of θ_κ around $\hat{z}$ axis with the spin-1/2 rotation operator

$$R(\theta) = \exp\left(-i\frac{\theta}{2}\sigma_z\right) = \begin{pmatrix} e^{-i\theta/2} & 0 \\ 0 & e^{+i\theta/2} \end{pmatrix}. \tag{5}$$

More explicitly, the vectorial part of the Bloch state, $|\boldsymbol{s}_p\rangle = e^{-i\boldsymbol{\kappa}\cdot\mathbf{r}}|\boldsymbol{\kappa}\rangle$ can be obtained from the initial state along the y-axis,

$$|\mathbf{s}_p^0\rangle = \frac{1}{\sqrt{2}} \begin{pmatrix} -is \\ 1 \end{pmatrix}, \tag{6}$$

by the rotation operation $|\mathbf{s}_p\rangle = R(\theta_\kappa)|\mathbf{s}_p^0\rangle$. Note that this rotation operation clearly resembles that of a two-component spinor describing the electron spin, but arising from the symmetry of the underlying honeycomb graphene lattice. In this regard, $|\mathbf{s}_p\rangle$ is often called "pseudo spin" in contrast to the real spin of electrons in graphene. The above operation also implies that the orientation of the pseudospin is tied to the $\boldsymbol{\kappa}$ vector. This is completely analogous to the real spin of massless fermions which always points along the direction of propagation. For $s = +1$, i.e., corresponding to the upper cone at $\mathbf{K}$ in Fig. 1, the states have pseudospin parallel to $\boldsymbol{\kappa}$, and thus correspond to the right-handed Dirac fermions. For $s = -1$, i.e. for the antiparticles in the lower cone, the situation is reversed, resulting in the left-handed Dirac antifermions.

So far our analysis is focused on the $\mathbf{K}$ point. It would be interesting to see what happens at the $\mathbf{K}'$ point. We apply a similar analysis at $\mathbf{K}'$, and the only difference is that now we expand the Hamiltonian around the $\mathbf{K}'$ point: $\mathbf{k} = \boldsymbol{\kappa} + \mathbf{K}'$. Then we obtain a new equation for $\mathbf{K}'$ from Eq. (1),

$$H = \hbar v_F \boldsymbol{\kappa} \cdot \bar{\boldsymbol{\sigma}}, \tag{7}$$

where $\bar{\boldsymbol{\sigma}}$ are the complex conjugate of the Pauli matrices $\boldsymbol{\sigma}$. This Hamiltonian is known to describe left-handed massless neutrinos. Therefore at $\mathbf{K}'$ the electron dynamics is again characterized by massless Dirac fermions, but with opposite helicity.

The chirality of the electrons in graphene has important implications on the electronic transport in graphene. In particular, a non-trivial Berry phase is associated with the rotation of the 1/2-pseudo spinor which plays a critical role to understand the unique charge transport in graphene and nanotubes, as first discussed in Ando et. al [5]'s theoretical work. For example, let us consider a scattering process $\boldsymbol{\kappa} \to \boldsymbol{\kappa}'$ due to a potential $V(\mathbf{r})$ with a range larger than the lattice constant in graphene, so that it does not induce an inter valley scattering between $\mathbf{K}$ and $\mathbf{K}'$ points. The resulting matrix element between these two states is given by [5, 33]

$$|\langle \boldsymbol{\kappa}'|V(\mathbf{r})|\boldsymbol{\kappa}\rangle|^2 = |V(\boldsymbol{\kappa} - \boldsymbol{\kappa}')|^2 \cos^2(\theta_{\kappa,\kappa'}/2), \tag{8}$$

where $\theta_{\kappa,\kappa'}$ is the angle between $\boldsymbol{\kappa}$ and $\boldsymbol{\kappa}'$, and the cosine term comes from the overlap of the initial and final spinors. A backscattering process corresponds to $\boldsymbol{\kappa} = -\boldsymbol{\kappa}'$. In this case, $\theta_{\kappa,\kappa'} = \pi$ and the matrix element vanishes. Therefore such backward scattering is completely suppressed. In terms of the pseudo spin argument, this back

scattering process can be described by rotating $|\boldsymbol{\kappa}\rangle$ by the rotating operation $R(\pi)$. For an atomically smooth potential the matrix element in Eq. (8) can be expressed

$$\langle \boldsymbol{\kappa}' | V(\mathbf{r}) | \boldsymbol{\kappa} \rangle \approx V(\boldsymbol{\kappa} - \boldsymbol{\kappa}') \langle \boldsymbol{\kappa} | R(\pi) | \boldsymbol{\kappa} \rangle. \tag{9}$$

Note that a π rotation of the 1/2 spinor always produces an orthogonal spinor to the original one, which makes this matrix element vanish.

The experimental significance of the Berry's phase of π was demonstrated by McEuen et al. [33] in single-wall carbon nanotubes (SWCNTs), which are essentially graphene rolled up into cylinders. The suppression of backscattering in metallic SWCNTs leads to a remarkably long electron mean free path on the order of a micron at room temperature [34].

The suppression of backward scattering can also be understood in terms of the Berry's phase induced by the pseudo spin rotation. In particular, for complete backscattering, Eq. (5) yields $R(2\pi) = e^{i\pi}$, indicating that rotation in $\boldsymbol{\kappa}$ by 2π leads to a change of the phase of the wave function $|\boldsymbol{\kappa}\rangle$ by π. This non-trivial Berry's phase may lead to non-trivial quantum corrections to the conductivity in graphene, where the quantum correction enhances the classical conductivity. This phenomena is called "anti-localization" in contrast to such quantum corrections in a conventional 2-dimensional (2D) system which lead to the suppression of conductivity in a weak localization. This can simply be explained by considering each scattering process with its corresponding complementary time-reversal scattering process. In a conventional 2D electron system such as in GaAs heterojunctions, the scattering amplitude and associated phase of each scattering process and its complementary time-reversal process are equal. This constructive interference in conventional 2D system leads to the enhancement of the backward scattering amplitude and thus results in the localization of the electron states. This mechanism is known as weak localization. In graphene, however, each scattering process and its time reversal pair have a phase difference by π between them due to the non-trivial Berry phase, stemming from 2π rotation of the pseudospin between the scattering processes of the two time reversal pairs. This results in a destructive interference between the time reversal pair to suppress the overal backward scattering amplitude, leading to a positive quantum correction in conductivity. These anti-weak localization phenomena in graphene have been observed experimentally [35].

While the existence of a non-trivial Berry's phase in graphene can be inferred indirectly from the aforementioned experiments, it can be directly observed in the quantum oscillations induced by a uniform external magnetic field [6, 7]. In a semi-classical picture, the electrons orbit along a circle in $\mathbf{k}$ space when subjected to a magnetic field. The Berry's phase of π produced by the 2π rotation of the wave vector manifests itself as a phase shift of the quantum oscillations, which will be the focus of the discussion of the next section.

4   Berry Phase in Magneto-oscillations

We now turn to the massless Dirac fermion described by Hamiltonian in Eq. (1). In a magnetic field, the Schrödinger equation is given by

$$\pm v_F (\mathbf{P} + e\mathbf{A}) \cdot \boldsymbol{\sigma} \psi(\mathbf{r}) = E \psi(\mathbf{r}), \tag{10}$$

where $\mathbf{P} = -i\hbar\bigtriangledown$, $\mathbf{A}$ is the magnetic vector potential, and $\psi(\mathbf{r})$ is a two-component vector

$$\psi(\mathbf{r}) = \begin{pmatrix} \psi_1(\mathbf{r}) \\ \psi_2(\mathbf{r}) \end{pmatrix}. \tag{11}$$

Here we use the Landau gauge $\mathbf{A}$: $\mathbf{A} = -By\hat{x}$ for a constant magnetic field $\mathbf{B}$ perpendicular to the $x-y$ plane. Then, taking only the $+$ sign in Eq. (10), this equation relates $\psi_1(\mathbf{r})$ and $\psi_2(\mathbf{r})$:

$$v_F(P_x - iP_y - eBy)\psi_2(\mathbf{r}) = E\psi_1(\mathbf{r}), \tag{12}$$
$$v_F(P_x + iP_y - eBy)\psi_1(\mathbf{r}) = E\psi_2(\mathbf{r}). \tag{13}$$

Substituting the first to the second equations above, we obtain the equation for $\psi_2(\mathbf{r})$ only

$$v_F^2(P^2 - 2eByP_x + e^2B^2y^2 - \hbar eB)\psi_2(\mathbf{r}) = E^2\psi_2(\mathbf{r}). \tag{14}$$

The eigenenergies of Eq. (14) can be found by comparing this equation with a massive carrier Landau system:

$$E_n^2 = 2n\hbar eBv_F^2, \tag{15}$$

where $n = 1, 2, 3...$ The constant $-\hbar eB$ shifts the LL's by half of the equal spacing between the adjacent LLs, and it also guarantees that there is a LL at $E = 0$, which has the same degeneracy as the other LLs. Putting these expressions together, the eigenenergy for a general LL can be written as [4]

$$E_n = sgn(n)\sqrt{2e\hbar v_F^2|n|B}, \tag{16}$$

where $n > 0$ corresponds to electron-like LLs and $n < 0$ corresponds to hole-like LLs. There is a single LL sitting exactly at $E = 0$, corresponding to $n = 0$, as a result of the chiral symmetry and the particle-hole symmetry.

The square root dependence of the Landau level energy on n, $E_n \propto \sqrt{n}$, can be understood if we consider the DOS for the relativistic electrons. The linear energy spectrum of 2D massless Dirac fermions implies a linear DOS given by

$$N(E) = \frac{E}{2\pi\hbar^2v_F^2}. \tag{17}$$

In a magnetic field, the linear DOS collapses into LLs, each of which has the same number of states $2eB/h$. As the energy is increased, there are more states available, so that a smaller spacing between the LLs is needed in order to have the same number of state for each LL. A linear DOS directly results in a square root distribution of the LLs, as shown in Fig. 3(c).

A wealth of information can be obtained by measuring the response of the 2D electron system in the presence of a magnetic field. One such measurement is done by passing current through the system and measuring the longitudinal resistivity ρ_{xx}. As we vary the magnetic field, the energies of the LLs change. In particular ρ_{xx} goes through one cycle of oscillations as the Fermi level moves from one LL DOS peak to the next as shown in Fig. 3(c). These are the so called Shubinikov de-Haas (SdH) oscillations. As we note in Eq. (15), the levels in a 2D massless Dirac fermion system, such as graphene, are shifted by a half-integer relative to the conventional

2D systems, which means that the SdH oscillations will have a phase shift of π, compared with the conventional 2D system.

The phase shift of π is a direct consequence of the Berry's phase associated with the massless Dirac fermion in graphene. To further elucidate how the chiral nature of an electron in graphene affects its motion, we resort to a semi-classical model where familiar concepts, such as the electron trajectory, provide us a more intuitive physical picture.

We consider an electron trajectory moving in a plane in a perpendicular magnetic field $\mathbf{B}$. The basic equation for the semi-classical approach is

$$\hbar\dot{\mathbf{k}} = -e(\mathbf{v} \times \mathbf{B}), \tag{18}$$

which simply says that the rate of change of momentum is equal to the Lorentz force. The velocity $\mathbf{v}$ is given by

$$\mathbf{v} = \frac{1}{\hbar}\,\bigtriangledown_{\mathbf{k}}\,\epsilon\,, \tag{19}$$

where ϵ is the energy of the electron. Since the Lorentz force is normal to $\mathbf{v}$, no work is done to the electron and ϵ is a constant of the motion. It immediately follows that electrons move along the orbits given by the intersections of constant energy surfaces with planes perpendicular to the magnetic fields.

Integration of Eq. (18) with respect to time yields

$$\mathbf{k}(t) - \mathbf{k}(0) = \frac{-eB}{\hbar}\left(\mathbf{R}(t) - \mathbf{R}(0)\right) \times \widehat{\mathbf{B}}, \tag{20}$$

where $\mathbf{R}$ is the position of the electron in real space, and $\widehat{\mathbf{B}}$ is the unit vector along the direction of the magnetic field $\mathbf{B}$. Since the cross product between $\mathbf{R}$ and $\widehat{\mathbf{B}}$ simply rotates $\mathbf{R}$ by $90°$ inside the plane of motion, Eq. (20) means that the electron trajectory in real space is just its k-space orbit, rotated by $90°$ about $\mathbf{B}$ and scaled by $\hbar/eB$.

It can be further shown that the angular frequency at which the electron moves around the intersection of the constant energy surface is given by

$$\omega_c = \frac{2\pi eB}{\hbar^2}\left(\frac{\partial a_k}{\partial \epsilon}\right)^{-1}, \tag{21}$$

where a_k is the area of the intersection in the k-space. For electrons having an effective mass m^*, we have $\epsilon = \hbar^2 k^2/2m^*$ and a_k is given by $\pi k^2 = 2\pi m^*\epsilon/\hbar^2$, while Eq. (21) reduces to $\omega_c = eB/m^*$. Comparing this equation with Eq. (21), we find

$$m^* = \frac{\hbar^2}{2\pi}\left(\frac{\partial a_k}{\partial \epsilon}\right), \tag{22}$$

which is actually the definition of the effective mass for an arbitrary orbit.

The quantization of the electron motion will restrict the available states and will give rise to quantum oscillations such as SdH oscillations. The Bohr-Sommerfeld quantization rule for a periodic motion is

$$\oint \mathbf{p} \cdot d\mathbf{q} = (n + \gamma)2\pi\hbar\,, \tag{23}$$

where $\mathbf{p}$ and $\mathbf{q}$ are canonically conjugate variables, n is an integer and the integration in Eq. (23) is for a complete orbit. The quantity γ will be discussed below.

For an electron in a magnetic field,

$$\mathbf{p} = \hbar\mathbf{k} - e\mathbf{A}, \qquad \mathbf{q} = \mathbf{R}, \tag{24}$$

so Eq. (23) becomes

$$\oint (\hbar\mathbf{k} - e\mathbf{A}) \cdot d\mathbf{R} = (n + \gamma)2\pi\hbar. \tag{25}$$

Substituting this equation into Eq. (20) and using Stokes' theorem, one finds

$$\mathbf{B} \cdot \oint \mathbf{R} \times d\mathbf{R} - \int_S \mathbf{B} \cdot d\mathbf{S} = (n + \gamma)\Phi_0, \tag{26}$$

where $\Phi_0 = 2\pi\hbar/e$ is the magnetic flux quanta. S is any surface in real space which has the electron orbit as the projection on the plane. Therefore the second term on the left hand side of Eq. (26) is just the magnetic flux $-\Phi$ penetrating the electron orbit. A closer inspection of the first term on the left hand side of Eq. (26) finds that it is 2Φ. Putting them together, Eq. (26) reduces to

$$\Phi = (n + \gamma)\Phi_0, \tag{27}$$

which simply means that the quantization rule dictates that the magnetic flux through the electron orbit has to be quantized.

Remember that the electron trajectory in real space is just a rotated version of its trajectory in k-space, scaled by $\hbar/eB$ (Eq. (20)). Let $a_k(\epsilon)$ be the area of the electron orbit at constant energy ϵ in k-space; then Eq. (20) becomes

$$a_k(\epsilon_n) = (n + \gamma)2\pi eB/\hbar, \tag{28}$$

which is the famous Onsager relation. This relation implicitly specifies the permitted energy levels ϵ_n (Landau Levels), which in general depend on the band structure dispersion relation $\epsilon(k)$.

The dimensionless parameter $0 \leq \gamma < 1$ is determined by the shape of the energy band structure. For a parabolic band, $\epsilon = \hbar^2 k^2/2m^*$, the nth LL has the energy $\epsilon_n = (n + 1/2)\hbar\omega_c$. Each LL orbit for an isotropic m^* in the plane perpendicular to the magnetic field B is a circle in k-space with a radius $k_n = \sqrt{2eB(n + 1/2)/\hbar}$. The corresponding area of an orbital in k-space for the nth LL is therefore

$$a_k(\epsilon_n) = \pi k_n^2 = (n + \frac{1}{2})2\pi eB/\hbar. \tag{29}$$

A comparison of this formula with Eq. (28) immediately yields

$$\gamma = \frac{1}{2}. \tag{30}$$

For a massless Dirac fermion in graphene which obeys a linear dispersion relation $\epsilon = \hbar v_F k$, the nth LL corresponds to a circular orbit with radius $k_n = \epsilon_n/\hbar v_F = \sqrt{2e|n|B/\hbar}$. The corresponding area is therefore

$$a_k(\epsilon_n) = \pi k_n^2 = |n|2\pi eB/\hbar. \tag{31}$$

This gives, for a semiclassical Shubnikov de Haas (SdH) phase,

$$\gamma = 0, \tag{32}$$

which differs from the γ for the conventional massive fermion by $\frac{1}{2}$.

The difference of $\frac{1}{2}$ in γ is a consequence of the chiral nature of the massless Dirac fermions in graphene. An electron in graphene always has the pseudospin $|\boldsymbol{s}_p\rangle$ tied to its wave vector $\mathbf{k}$. The electron goes through the orbit for one cycle, $\mathbf{k}$, as well as the pseudospin attached to the electrons. Both go through a rotation of 2π at the same time. Much like a physical spin, a 2π adiabatic rotation of pseudospin gives a Berry's phase of π [5]. This is exactly where the $\frac{1}{2}$ difference in γ comes from.

The above analysis can be generalized to systems with an arbitrary band structure. In general, γ can be expressed in terms of the Berry's phase, ϕ_B, for the electron orbit:

$$\gamma - \frac{1}{2} = -\frac{1}{2\pi}\phi_B \,. \tag{33}$$

For any electron orbits which surround a disconnected electronic energy band, as is the case for a parabolic band, this phase is zero, and we arrive at Eq. (30). A non-trivial Berry's phase of π results if the orbit surrounds a contact between the bands, and the energies of the bands separate linearly in $\mathbf{k}$ in the vicinity of the band contact. In monolayer graphene, these requirements are fulfilled because the valence band and conduction band are connected by $\mathbf{K}$ and $\mathbf{K}'$, and the energy dispersion is linear around these points. This special situation again leads to a $\gamma = 0$ in graphene (in fact, $\gamma = 0$ and $\gamma = \pm 1$ are equivalent). Note that this non-trivial γ is only for monolayer graphene; in contrast for bilayer graphene, whose band contact points at the charge neutrality point have a quadratic dispersion relation, a conventional $\gamma = 1/2$ is obtained.

γ can be probed experimentally by measuring the quantum oscillation of the 2D system in the presence of a magnetic field, where γ is identified as the phase of such oscillations. This becomes evident when we explicitly write the oscillatory part of the quantum oscillations, e.g., as for the SdH oscillation of the electrical resistivity, $\Delta\rho_{xx}$ [7]

$$\Delta\rho_{xx} = R(B,T)\cos\left[2\pi\left(\frac{B_F}{B} - \gamma\right)\right]. \tag{34}$$

Here we only take account of the first harmonic, in which $R(B,T)$ is the amplitude of the SdH oscillations and B_F is the frequency in units of $1/B$, which can be related to the 2D charge carrier density n_s by

$$B_F = \frac{n_s h}{g_s e} \,, \tag{35}$$

where $g_s = 4$ accounts for the spin and valley degeneracies of the LLs. The relation $\gamma = 1/2$ (for a parabolic band) and $\gamma = 0$ (for graphene) produces a phase difference of π between the SdH oscillation in the two types of 2D systems. In the extreme quantum limit, the SdH oscillations evolve into the quantum Hall effect, a remarkable macroscopic quantum phenomenon characterized by a precisely quantized Hall resistance and zeros in the longitudinal magneto-resistance. The additional Berry's phase of π manifests itself as a half-integer shift in the quantization condition, and leads to an unconventional quantum Hall effect. In the quantum Hall regime, graphene

thus exhibits a so-called "half-integer" shifted quantum Hall effect, where the filling fraction is given by $\nu = g_s(n + 1/2)$ for integer n. Thus, at this filling fraction $\rho_{xx} = 0$, while the Hall resistivity exhibits quantized plateaus at

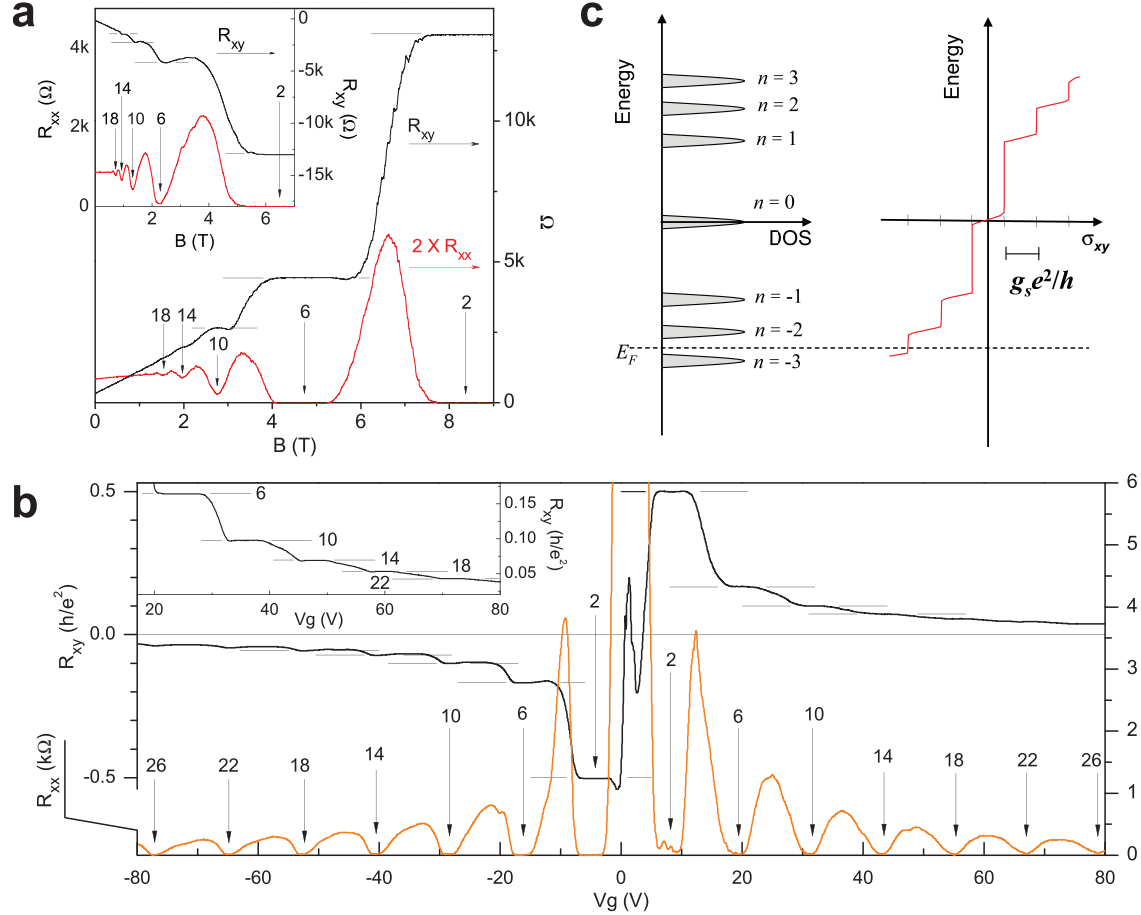$$\rho_{xy}^{-1} = \frac{e^2}{h} g_s \left(n + \frac{1}{2} \right). \tag{36}$$

Figure 3: Quantized magnetoresistance and Hall resistance of a graphene device. (a) Hall resistance (black) and magnetoresistance (red) measured in a monolayer graphene device at $T = 30$ mK and $V_g = 15$ V. The vertical arrows and the numbers on them indicate the values of B and the corresponding filling factor ν of the quantum Hall states. The horizontal lines correspond to $h/\nu e^2$ values. The QHE in the electron gas is demonstrated by at least two quantized plateaus in R_{xy} with vanishing R_{xx} in the corresponding magnetic field regime. The inset shows the QHE for a hole gas at $V_g = -4$ V, measured at 1.6 K. The quantized plateau for filling factor $\nu = 2$ is well-defined and the second and the third plateaus with $\nu = 6$ and 10 are also resolved. (b) The Hall resistance (black) and magnetoresistance (orange) as a function of gate voltage at fixed magnetic field $B = 9$ T, measured at 1.6 K. The same convention as in (a) is used here. The upper inset shows a detailed view of high filling factor R_{xy} plateaus measured at 30 mK. (c) A schematic diagram of the Landau level density of states (DOS) and corresponding quantum Hall conductance (σ_{xy}) as a function of energy. Note that in the quantum Hall states, $\sigma_{xy} = -R_{xy}^{-1}$. The LL index n is shown next to the DOS peak. In our experiment, the Fermi energy E_F can be adjusted by the gate voltage, and R_{xy}^{-1} changes by an amount of $g_s e^2/h$ as E_F crosses a LL. Reproduced from Ref. [7].

The experimental observation of the quantum Hall effect and Berry's phase in graphene were first reported in Novoselov *et al.* [6] and Zhang *et al.* [7]. Figure 3a shows R_{xy} and R_{xx} of a single layer graphene sample as a function of magnetic field B at a fixed gate voltage $V_g > V_{Dirac}$. The overall positive R_{xy} indicates that the contribution to R_{xy} is mainly from electrons. At high magnetic field, $R_{xy}(B)$ exhibits plateaus and R_{xx} is vanishing, which is the hallmark of the QHE. At least two well-defined plateaus with values $(2e^2/h)^{-1}$ and $(6e^2/h)^{-1}$, followed by a developing $(10e^2/h)^{-1}$ plateau, are observed before the QHE features are transformed into Shubnikov de Haas (SdH) oscillations at lower magnetic field. The quantization of R_{xy} for these first two plateaus is better than 1 part in 10^4, with a precision within the instrumental uncertainty. In recent experiments [36], this limit is now at the accuracy of the 10^{-9} level. We observe the equivalent QHE features for holes ($V_g < V_{Dirac}$) with negative R_{xy} values (Fig. 3a, inset). Alternatively, we can probe the QHE in both electrons and holes by fixing the magnetic field and by changing V_g across the Dirac point. In this case, as V_g increases, first holes ($V_g < V_{Dirac}$) and later electrons ($V_g > V_{Dirac}$) are filling successive Landau levels and thereby exhibit the QHE. This yields an antisymmetric (symmetric) pattern of R_{xy} (R_{xx}) in Fig. 3b, with R_{xy} quantization accordance to

$$R_{xy}^{-1} = \pm g_s(n + \frac{1}{2})e^2/h \,, \qquad (37)$$

where n is a non-negative integer, and +/- stands for electrons and holes, respectively. This quantization condition can be translated to the quantized filling factor, ν, in the usual QHE language. Here in the case of graphene, $g_s = 4$, accounting for 2 by the spin degeneracy and 2 by the sub-lattice degeneracy, equivalent to the **K** and **K**′ valley degeneracy under a magnetic field.

The observed QHE in graphene is distinctively different from the "conventional" QHEs because of the additional half-integer in the quantization condition (Eq. (37)). This unusual quantization condition is a result of the topologically exceptional electronic structure of graphene. The sequence of half-integer multiples of quantum Hall plateaus has been predicted by several theories which combine "relativistic" Landau levels with the particle-hole symmetry of graphene [37, 38, 39]. This can be easily understood from the calculated LL spectrum (Eq. (16)) as shown in Fig. 3(c). Here we plot the density of states (DOS) of the g_s-fold degenerate (spin and sublattice) LLs and the corresponding Hall conductance ($\sigma_{xy} = -R_{xy}^{-1}$, for $R_{xx} \to 0$) in the quantum Hall regime as a function of energy. Here σ_{xy} exhibits QHE plateaus when E_F (tuned by V_g) falls between LLs, and jumps by an amount of $g_s e^2/h$ when E_F crosses a LL. Time reversal invariance guarantees particle-hole symmetry and thus σ_{xy} is an odd function in energy across the Dirac point [4]. However, in graphene, the $n = 0$ LL is robust, i.e., $E_0 = 0$ regardless of the magnetic field, provided that the sublattice symmetry is preserved[4]. Thus the first plateaus of R_{xy}^{-1} for electrons ($n = 1$) and holes ($n = -1$) are situated exactly at $g_s e^2/2h$. As E_F crosses the next electron (hole) LL, R_{xy}^{-1} increases (decreases) by an amount of $g_s e^2/h$, which yields the quantization condition in Eq. (37).

A consequence of the combination of time reversal symmetry with the novel Dirac point structure can be viewed in terms of Berry's phase arising from the band degeneracy point. A direct implication of Berry's phase in graphene is discussed in the context of the quantum phase of a spin-1/2 pseudo-spinor that describes the

sublattice symmetry [5]. This phase is already implicit in the half-integer shifted quantization rules of the QHE.

The linear energy dispersion relation also leads to a linearly vanishing 2D density of states near the charge neutrality point (CNP) at $E = 0$, $\rho_{2D} \propto |\epsilon_F|$. This differs from that for conventional parabolic 2D systems in which the density of states, at least in the single particle picture, is constant, leading to a decrease in the ability of charge neutral graphene to screen electric fields. Finally, the sublattice symmetry endows the quasiparticles with a conserved quantum number and chirality, corresponding to the projection of the pseudospin on the direction of motion [9]. In the absence of scattering which mixes the electrons in the graphene valleys, pseudospin conservation forbids backscattering in graphene [5], momentum reversal being equivalent to the violation of pseudospin conservation. This absence of backscattering has been advanced as an explanation for the experimentally observed unusually long mean free path of carriers in metallic as compared with semiconducting nanotubes [33].

5   Pseudospin and Klein Tunneling in graphene

The observation of electron and hole puddles in charge neutral, substrate supported graphene confirmed theoretical expectations [42] that transport at charge neutrality is dominated by charged impurity-induced inhomogeneities. The picture of transport at the Dirac point is as a result of conducting puddles separated by a network of p-n junctions. Understanding the properties of graphene p-n junctions is thus crucial to quantitative understanding of the minimal conductivity, a problem that has intrigued experimentalists and theorists alike [6, 42]. Describing transport in the inhomogeneous potential landscape of the CNP requires introduction of an additional spatially varying electrical potential into Eq. (1) in the previous section; transport across a p-n junction corresponds to this varying potential crossing zero. Because graphene carriers have no mass, graphene p-n junctions provide a condensed matter analogue of the so called "Klein tunneling" problem in quantum electro-dynamics (QED). The first part of this section will be devoted to the theoretical understanding of ballistic and diffusive transport across such as barrier.

In recent years, substantial effort has been devoted to improving graphene sample quality by eliminating unintentional inhomogeneity. Some progress in this direction has been made by both suspending graphene samples [43, 44] as well as by transferring graphene samples to single crystal hexagonal boron nitride substrates [45]. These techniques have succeeded in lowering the residual charge density present at charge neutrality, but even the cleanest samples are not ballistic on length scales comparable to the sample size (typically $\gtrsim 1~\mu$m). An alterative approach is to try to restrict the region of interest being studied by the use of local gates.

Graphene's gapless spectrum allows the fabrication of adjacent regions of positive and negative doping through the use of local electrostatic gates. Such heterojunctions offer a simple arena in which to study the peculiar properties of graphene's massless Dirac charge carriers, including chirality [46, 9] and emergent Lorentz invariance [48]. Technologically, graphene p-n junctions are relevant for various electronic devices, including applications in conventional analog and digital circuits as well as novel electronic devices based on electronic lensing. In the latter part of this review, we will discuss current experimental progress towards such gate-engineered

coherent quantum graphene devices.

The approach outlined in the previous section requires only small modifications to apply the approach to the case of carrier transport across graphene heterojunctions. While the direct calculation for the case of graphene was done by Katsnelson et al. [9], a similar approach taking into account the chiral nature of carriers was already discussed a decade ago in the context of electrical conduction in metallic carbon nanotubes [5]. In low dimensional graphitic systems, the free particle states described by Eq. (1) are chiral, meaning that their pseudospin is parallel (antiparallel) to their momentum for electrons (holes). This causes a suppression of backscattering in the absence of pseudospin-flip nonconserving processes, leading to the higher conductances of metallic over semiconducting carbon nanotubes [33]. To understand the interplay between this effect and Klein tunneling in graphene, we introduce external potentials $\boldsymbol{A}(\boldsymbol{r})$ and $U(\boldsymbol{r})$ in the Dirac Hamiltonian,

$$\hat{H} = v_F \boldsymbol{\sigma} \cdot (-i\hbar\boldsymbol{\nabla} - e\boldsymbol{A}(\boldsymbol{r})) + U(\boldsymbol{r}). \tag{38}$$

In the case of a 1-dimensional (1D) barrier, $U(\boldsymbol{r}) = U(x)$, at zero magnetic field, and the momentum component parallel to the barrier, p_y, is conserved. As a result, electrons normally incident on a graphene p-n junction are forbidden from scattering obliquely by the symmetry of the potential, while chirality forbids them from scattering directly backwards: the result is perfect transmission as holes [9], and this is what is meant by Klein tunneling in graphene (see (Fig. 4) (a)). The rest of this review is concerned with gate induced p-n junctions in graphene; however, the necessarily transmissive nature of graphene p-n junctions is crucial for understanding the minimal conductivity and supercritical Coulomb impurity problems in graphene, as well as playing a role in efforts to confine graphene quantum particles. Moreover, p-n junctions appear in the normal process of contacting and locally gating graphene, both of which are indispensable for electronics applications.

Even in graphene, an atomically sharp potential cannot be created in a realistic sample. Usually, the distance to the local gate, which is isolated from the graphene by a thin dielectric layer determines the length scale on which the potential varies. The resulting transmission problem over a Sauter-like potential step in graphene was solved by Cheianov and Fal'ko [46]. Substituting the Fermi energy for the potential energy difference $\varepsilon - U(x) = \hbar v_f k_f(x)$ and taking into account the conservation of the momentum component $p_y = \hbar k_F \sin\theta$ parallel to the barrier, they obtained a result, valid for $\theta \ll \pi/2$, that is nearly identical to that of Sauter [47]:

$$k_F(x) = \begin{cases} -k_F/2 & x < 0, \\ Fx & 0 \leq x \leq L, \\ k_F/2 & x > L. \end{cases} \qquad |T|^2 \sim e^{-2\pi^2 \frac{hv_F}{F\lambda_F^2}\sin^2\theta}, \tag{39}$$

As in the massive relativistic problem in one-dimension, the transmission is determined by evanescent transport in classically forbidden regions where $k_x(x)^2 = k_F(x)^2 - p_y^2 < 0$ (Fig.4). The only differences between the graphene case and the one dimensional, massive relativistic case are the replacement of the speed of light by the graphene Fermi velocity, the replacement of the Compton wavelength by the Fermi wavelength, and the scaling of the mass appearing in the transmission by the sine of the incident angle. By considering different angles of transmission in the barrier problem in two dimensional graphene, then, one can access both the Klein and Sauter regimes of $T \sim 1$ and $T \ll 1$.
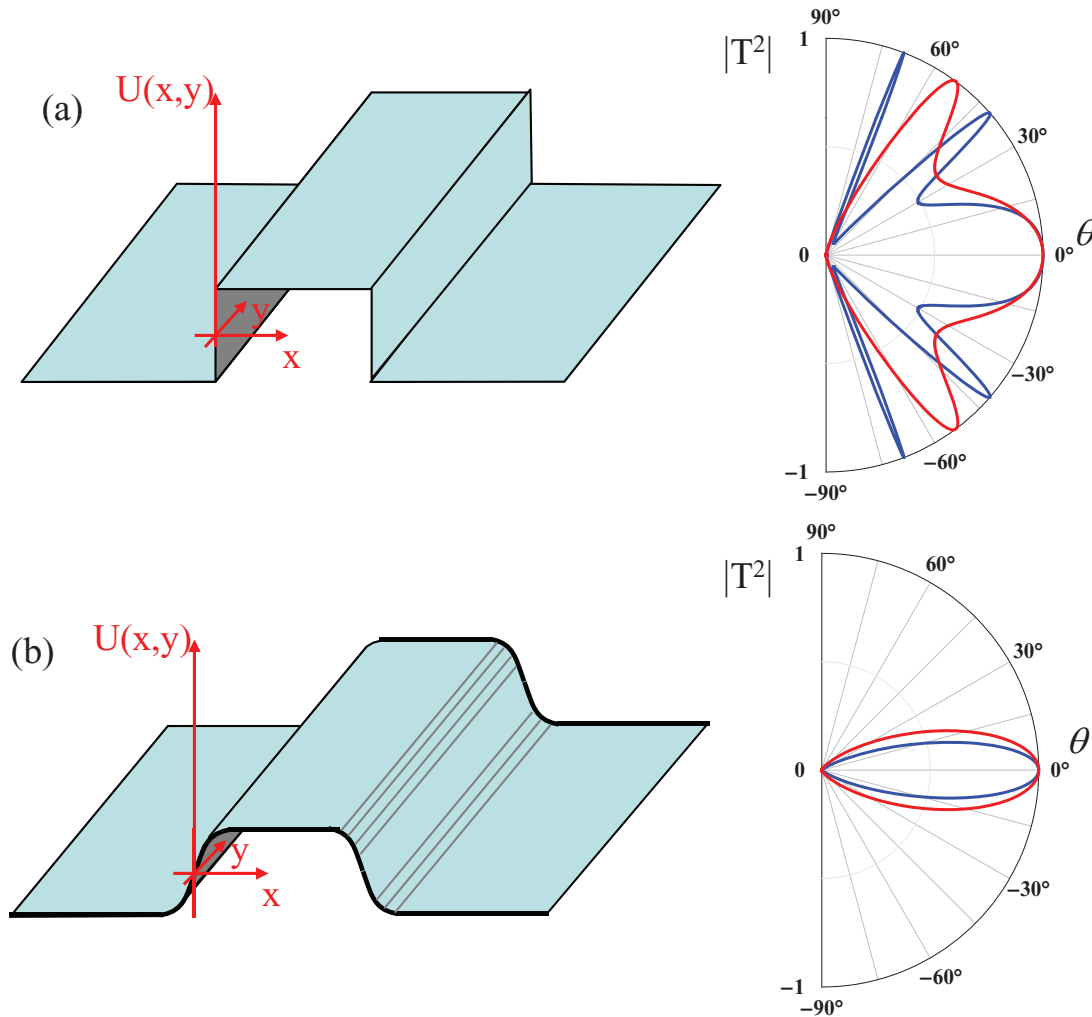
Figure 4: Potential landscape and angular dependence of quasiparticle transmission through (a) an atomically sharp pnp barrier and (b) an electrostatically generated smooth pnp barrier in graphene, with their respective angle-dependent transmission probabilities $|T|^2$. Red and blue lines correspond to different densities in the locally gated region.

The current state of the experimental art in graphene does not allow for injection of electrons with definite p_y [8, 49]. Instead, electrons impinging on a p-n junction have a random distribution of incident angles due to scattering in the diffusive graphene leads. Equation 39 implies that in realistically sharp p-n junctions, these randomly incident electrons emerge from the p-n junction as a collimated beam, with most off-normally incident carriers being scattered; transmission through multiple p-n junctions leads to further collimation. Importantly, even in clean graphene, taking into account the finite slope of the barrier yields qualitatively different results for the transmission: just as in the original Klein problem, the sharp potential step [9] introduces pathologies—in the case of graphene, high transmission at $\theta \neq 0$—which disappear in the more realistic treatment [46].

Transport measurements across single p-n junctions, or a pnp junction in which transport is not coherent, can at best provide only indirect evidence for Klein tun-

neling by comparison of the measured resistance of the p-n junction. Moreover, because such experiments probe only incident-angle averaged transmission, they cannot experimentally probe the structure $T(\theta)$. Thus, although the resistance of nearly ballistic p-n junctions are in agreement with the ballistic theory, to show that angular collimation occurs, or that there is perfect transmission at normal incidence, requires a different experiment. In particular, there is no way to distinguish perfect transmission at $\theta = 0$ from large transmission at all angles, begging the question of whether "Klein tunneling" has any observable consequences outside the context of an angle resolved measurement or its contribution to bulk properties such as the minimal conductivity. In fact, as was pointed out by Shytov et al. [50], an experimental signature of this phenomenon should manifest itself as a sudden phase shift at finite magnetic field in the transmission resonances in a ballistic, phase coherent, graphene pnp device.

Although graphene p-n junctions are transmissive when compared with p-n junctions in gapfull materials (or gapless materials in which backscattering is allowed, such as bilayer graphene), graphene p-n junctions are sufficiently reflective, particularly for obliquely incident carriers, to cause transmission resonances due to Fabry-Perot interference. However, in contrast to the canonical example from optics, or to one dimensional electronic analogues, the relative phase of interfering paths in a ballistic, phase coherent pnp (or npn) graphene heterojunction can be tuned by applying a magnetic field. For the case where the junction width is only somewhat shorter than the mean free path in the local gate region (LGR), $L \lesssim \ell_{LGR}$, the Landauer formula for the oscillating part of the conductance trace can be derived from the ray tracing diagrams in Fig. 5(d),

$$G_{osc} = e^{-2L/l_{LGR}} \frac{4e^2}{h} \sum_{k_y} 2|T_+|^2 |T_-|^2 R_+ R_- \cos\left(\theta_{WKB}\right), \qquad (40)$$

in which $T_\pm$ and $R_\pm$ are the transmission and reflection amplitudes at $x = \pm L/2$, θ_{WKB} is the semiclassical phase difference accumulated between the junctions by interfering trajectories, and ℓ_{LGR} is a fitting parameter which controls the amplitude of the oscillations.

At zero magnetic field, particles are incident at the same angle on both junctions, and the Landauer sum in Eq. (40) is dominated by the modes for which both transmission and reflection are nonnegligible, so neither normal nor highly oblique modes contribute. Instead, the sum is dominated by modes with finite k_y, peaked about $k_y = \pm\sqrt{F/(\ln{(3/2)}\pi\hbar v_F)}$, where F is the electric force in the pn junction region. As the magnetic field increases, cyclotron bending favors the contribution of modes with $k_y = 0$, which are incident on the junctions at angles with the same magnitude but opposite sign (Fig. 5(c)). If perfect transmission at zero angle exists, then analyticity of the scattering amplitudes demands that the reflection amplitude changes sign as the sign of the incident angle changes [50], thereby causing a π shift in the reflection phase. This effect can also be described in terms of the Berry phase: the closed momentum space trajectories of the modes dominating the sum at low field and high k_y do not enclose the origin, while those at intermediate magnetic fields and $k_y \sim 0$ do. As a consequence, the quantization condition leading to transmission resonances is different due to the inclusion of the Berry phase when the trajectories surround the topological singularity at the origin, leading to

a phase shift in the observed conductance oscillations as the phase shift containing trajectories begin to dominate the Landauer sum in Eq. (40).

Experimental realization of the coherent electron transport in pnp (as well as npn) graphene heterojunctions was reported by Young and Kim [8]. The key experimental innovations were to use an extremely narrow ($\lesssim$ 20 nm wide) top gate, creating a Fabry Perot cavity between p-n junctions smaller than the mean free path, which was $\sim$ 100 nm in the samples studied. Figure 5(a) shows the layout of a graphene heterojunction device controlled by both top gate voltage (V_{TG}) and back gate voltage (V_{BG}). The conductance map shows clear periodic features in the presence of p-n junctions; these features appear as oscillatory features in the conductance as a function of V_{TG} at fixed V_{BG} (Fig. 5(b)). For the electrostatics of the devices presented in this device, the magnetic field at which this π phase shift, due to the Berry phase at the critical magnetic field discussed above, is expected to occur in the range $B^* = 2\hbar k_y/eL \sim$250–500 mT, in agreement with experimental data which show an abrupt phase shift in the oscillations at a few hundred mT (Fig. 5(f)). Experiments can be matched quantitatively to the theory by calculation of Eq. (40) for the appropriate potential profile, providing confirmation of the Klein tunneling phenomenon in graphene. As the magnetic field increases further, the ballistic theory predicts the disappearance of the Fabry-Perot conductance oscillations as the cyclotron radius shrinks below the distance between p-n junctions, $R_c \lesssim L$, or B$\sim$2 T for our devices (Fig. 5(e)). The qualitative understanding of these behaviors can be explained in the semiclassical way (Fig. 5(c)): with increasing B, the dominant modes at low magnetic field (blue) give way to phase-shifted modes with negative reflection amplitude due to the inclusion of the non-trivial Berry phase (orange), near $k_y = 0$. The original finite k_y modes are not yet phase shifted at the critical magnetic field B_c, above which the non-trivial Berry phase shift π (green) appears. But owing to collimation, these finite k_y modes no longer contribute to the oscillatory conductance.

There is an apparent continuation of the low magnetic field Fabry-Perot (FP) oscillations to Shubnikov-de Haas (SdH) oscillations at high magnetic fields. Generally, the FP oscillations tend to be suppressed at high magnetic fields as the cyclotron orbits get smaller than the junction size. On the other hand, disorder mediated SdH oscillations become stronger at high magnetic field owing to the large separation between Landau levels. The observed smooth continuation between these two oscillations does not occur by chance. FP oscillations at magnetic fields higher than the phase shift are dominated by trajectories with $k_y = 0$; similarly, SdH oscillations, which can be envisioned as cyclotron orbits beginning and ending on the same impurity, must also be dominated by $k_y = 0$ trajectories. The result is a seamless crossover from FP to SdH oscillations. This is strongly dependent on the disorder concentration: for zero disorder, SdH oscillations do not occur, while for very strong disorder SdH oscillations happen only at high fields and FP oscillations do not occur due to scattering between the p-n junctions. For low values of disorder, such that SdH oscillations appear at fields much smaller than the phase shift magnetic field, B_c, the two types of coherent oscillations could in principle coexist with different phases. The role of disorder in the FP-SdH crossover has only begun to be addressed experimentally [8].
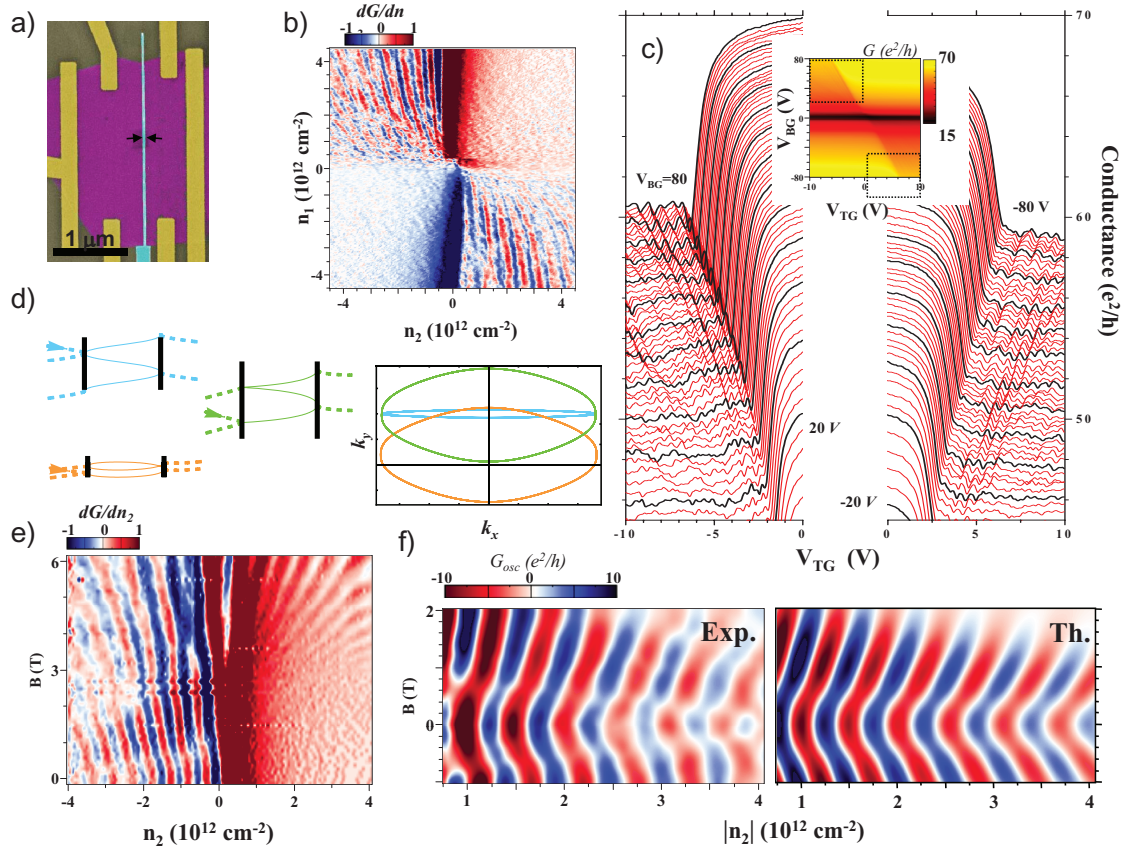
Figure 5: (a) Scanning electron microscope image of a typical graphene heterojunction device. Electrodes, graphene and top gates are represented by yellow, purple and cyan, respectively. (b) A differential transconductance map of the device as a function of densities n_2 and n_1, corresponding to the locally gated region (LGR) and out side the LGR, i.e. graphene lead (GL) region, respectively. Interference fringes appear in the presence of pn junctions, which define the Fabry-Perot cavity. (c) Inset: Conductance map of the device in the back gate and top gate voltages (V_{BG}-V_{TG}) plane. The main panels show cuts through this color map in the regions indicated by the dotted lines in the inset, showing the conductance as a function of V_{TG} at fixed V_{BG}. Traces are separated by a step in V_{BG} of 1 V, starting from 80V with traces taken at integer multiples of 5 V in black. (d) Schematic diagram of trajectories contributing to quantum oscillations in real and momentum space. (e) Magnetic-field and density dependence of the transconductance dG/dn_2 for $n_1 > 0$ is fixed. Note that the low field oscillatory features from FP resonance only appear for $n_2 < 0$ where there is pnp junction forms. (f) Oscillating part of the conductance at V_{BG} =50 V for low fields. G_{osc} as extracted from the experimental data over a wide range of densities and magnetic fields (left) matches the behavior predicted by a theory containing the phase shift due to Klein tunneling [50] (right). Reproduced from Ref. [8].

6   Conclusions

In this chapter, we discuss the role of pseudospin in electronic transport in graphene. We demonstrate a variety of new phenomena which stem from the effectively relativistic nature of the electron dynamics in graphene, where the pseudospin is aligned with two-dimensional momentum. Our main focus were two major topics: (i) the non-conventional, half-integer shifted filling factors for the quantum Hall effect (QHE)

Matière de Dirac, Vol. XVIII, 2014   Graphene and Relativistic Quantum Physics   19

and the peculiar magneto-oscillation where one can directly probe the existence of a non-trivial Berry's phase, and (ii) Klein tunneling of chiral Dirac fermions in a graphene lateral heterojunction.

Employing unusual filling factors in QHE in single layer graphene samples as an example, we demonstrated that the observed quantization condition in graphene is described by half integer rather than integer values, indicating the contribution of the non-trivial Berry's phase. The half-integer quantization, as well as the measured phase shift in the observed magneto-oscillations, can be attributed to the peculiar topology of the graphene band structure with a linear dispersion relation and a vanishing mass near the Dirac point, which is described in terms of effectively "relativistic" carriers as shown in Eq. (1). The unique behavior of electrons in this newly discovered $(2 + 1)$-dimensional quantum electrodynamics system not only opens up many interesting questions in mesoscopic transport in electronic systems with non-zero Berry's phase but may also provide the basis for novel carbon based electronics applications.

The development and current status of electron transport in graphene heterojunction structures were also reviewed. In these lateral heterojunction devices, the unique linear energy dispersion relation and concomitant pseudospin symmetry are probed via the use of local electrostatic gates. Mimicking relativistic quantum particle dynamics, electron waves passing between two regions of graphene with different carrier densities will undergo strong refraction at the interface, producing an experimental realization of the century-old Klein tunneling problem of relativistic quantum mechanics. Many theoretical and experimental discussions were presented here, including the peculiar graphene p-n and *pnp* junction conduction in the diffusive and ballistic regimes. Since electrons are charged, a magnetic field can couple to them and magnetic field effects can be studied. In particular, in a coherent system, the electron waves can also interfere, producing quantum oscillations in the electrical conductance, which can be controlled through the application of both electric and magnetic fields. A clear indication of a phase shift of π in the magnetoconductance clearly indicates again the existence of a non-trivial Berry's phase associated with the pseudo-spin rotation during the Klein tunneling process.

References

[1] Wallace, P. R.: Phys. Rev. **71**, 622 (1947).

[2] DiVincenzo, D. P., and Mele, E. J.: Phys. Rev. B **29**, 1685 (1984).

[3] Semenoff, G. W.: Phys. Rev. Lett. **53**, 2449 (1984).

[4] Haldane, F. D. M.: Phys. Rev. Lett. **61**, 2015 (1988).

[5] Ando, T., Nakanishi, T., and Saito, R.: J. Phys. Soc. Jpn **67**, 2857 (1998).

[6] Novoselov, K. S., Geim, A. K., Morozov, S. V., Jiang, D., Katsnelson, M. I., Grigorieva, I. V., Dubonos, S. V., and Firsov, A. A.: Nature **438**, 197 (2005).

[7] Zhang, Y., Tan, Y.-W., Stormer, H. L., and Kim, P.: Nature **438**, 201 (2005).

[8] Young, A. F., and Kim, P.: Nat. Phys. **5**, 222 (2009).

[9] Katsnelson, M. I., Novoselov, K. S., and Geim, A. K.: Nat. Phys. **2**, 620 (2006).

[10] Wilson, M.: Physics Today **1**, 21 (2006).

[11] Boehm, H. P., Clauss, A., Fischer, G. O., Hofmann, U.: Z. anorg. allg. Chem. **316**, 119 (1962).

[12] Land, T. A., Michely, T., Behm, R. J., Hemminger, J. C., Comsa, G.: Sur. Sci. **264**, 261–270 (1992).

[13] Krishnan, A., Dujardin, E., Treacy, M. M. J., Hugdahl, J., Lynum, S., and Ebbesen, T. W.: Nature **388**, 451 (1997).

[14] Berger, C., Song, Z. M., Li, T. B., Li, X. B., Ogbazghi, A. Y., Feng, R., Dai, Z. T., Marchenkov, A. N., Conrad, E. H., First, P. N., and de Heer, W. A.: J. Phys. Chem. B **108**, 19912 (2004).

[15] de Heer, W. A., Berger, C., Ruan, M., Sprinkle, M., Li, X., Yike Hu, Zhang, B., Hankinson, J., Conrad, E.H.: PNAS **108**, (41) 16900 (2011).

[16] Bae, S. *et. al.*: Nature Nanotech. **5**, 574 (2010).

[17] Yamamoto, M., Obata, S., and Saiki, K.: Surface and Interface Analysis **42**, 1637 (2010).

[18] Zhang, L. *et. al.*: Nano Lett. **12**, 1806 (2012).

[19] Frindt, R. F.: Phys. Rev. Lett. **28**, 299 (1972).

[20] Ohashi, Y., Hironaka, T., Kubo, T., and Shiki, K.: Tanso 1997, 235 (1997).

[21] Itoh, H., Ichinose, T., Oshima, C., and Ichinokawa, T.: Surf. Sci. Lett. **254**, L437 (1991).

[22] Viculis, L. M., Jack, J. J., and Kaner, R. B.: Science **299**, 1361 (2003).

[23] Ebbensen, W., and Hiura, H.: Adv. Mater. **7**, 582 (1995).

[24] Lu, X., Huang, H., Nemchuk, N., and Ruoff, R.: Appl. Phys. Lett. **75**, 193 (1999).

[25] Lu, X., Yu, M., Huang, H., and Ruoff, R.: Nanotechnology **10**, 269 (1999).

[26] Dujardin, E., Thio, T., Lezec, H., and Ebbesen, T. W.: Appl. Phys. Lett. **79**, 2474 (2001).

[27] Novoselov, K. S., Geim1, A. K., Morozov, S. V., Jiang, D., Zhang, Y., Dubonos, S. V., Grigorieva, I. V., Firsov, A. A.: Science **306**, 666 (2004).

[28] Zhang, Y., Small, J. P., Pontius, W. V., and Kim, P.: App. Phys. Lett. **86**, 073104 (2005).

[29] Bunch, J. S., Yaish, Y., Brink, M., Bolotin, K., and McEuen, P. L.: Nano Lett. **5**, 287 (2005).

[30] Novoselov, K. S., Jiang, D., Schedin, F., Booth, T. J., Khotkevich, V. V., Morozov, S. V., and Geim, A. K.: PNAS **102**, 10451 (2005).

[31] Blake, P., Hill, E. W., Castro Neto, A. H., Novoselov, K. S., Jiang, D., Yang, R., Booth, T. J., and Geim, A. K.: Appl. Phys. Lett. **91**, 063124 (2007).

[32] Slonczewski, J. C., and Weiss, P. R.: Phys. Rev. **109**, 272 (1958).

[33] McEuen, P.L., Bockrath, M., Cobden, D.H., Yoon, Y.-G., and Louie, S.G.: Phys. Rev. Lett. **83**, 5098 (1999).

[34] Purewal, M. S., Hong, B. H., Ravi, A., Chandra, B., Hone, J., and Kim, P.: Phys. Rev. Lett. **98**, 196808 (2006).

[35] Tikhonenko, F. V., Horsell, D. W., Gorbachev, R. V., and Savchenko, A. K.: Phys. Rev. Lett. **100**, 056802 (2008).

[36] Tzalenchuk1, A., Lara-Avila, S., Kalaboukhov, A., Paolillo, S., Syvajarvi, M., Yakimova, R., Kazakova, O., Janssen, T. J. B. M., Fal'ko, V., and Kubatkin, S.: Nature Nano. **5**, 186 (2010).

[37] Zheng, Y. S., and Ando, T.: Phys. Rev. B **65**, 245420 (2002).

[38] Gusynin, V. P., and Sharapov, S. G.: Phys. Rev. Lett. **95**, 146801 (2005).

[39] Peres, N. M. R., Guinea, F., and Neto, A. H. C.: Phys. Rev. B **73**, 125411 (2006).

[40] Morozov, S. V., Novoselov, K. S., Schedin, F., Jiang, D., Firsov, A. A., and Geim, A. K.: Phys. Rev. B **72**, 201401 (R) (2005).

[41] Zhang, Y., Small, J. P., Amori, M. E. S., and Kim, P.: Phys. Rev. Lett. **94**, 176803 (2005).

[42] Hwang, E. H., Adam, S., and Das Sarma, S.: Phys. Rev. Lett. **98**, 186806 (2007).

[43] Bolotin, K. I., Sikes, K. J., Jiang, Z., Fundenberg, G., Hone, J., Kim, P., and Stormer, H. L.: Sol. State Comm. **146**, 351 (2008).

[44] Du, X., Skachko, I., Barker, A., and Andrei, E. Y.: Nature Nano. **3**, 491 (2008).

[45] Dean, C.R., Young, A.F., Meric, I., Lee, C., Wang, L., Sorgenfrei, S., Watanabe, K., Taniguchi, T., Kim, P., Shepard, K.L., and Hone, J.: Nature Nano. **5**, 722 (2010).

[46] Cheianov, V. V., and Fal'ko, V. I.: Phys. Rev. B **74**, 041403 (2006).

[47] Sauter, F.: Zeitschrift für Physik A Hadrons and Nuclei **69**, 742 (1931).

[48] Lukose, V., Shankar, R., and Baskaran, G.: Phys. Rev. Lett. **98**, 116802 (2007).

[49] Huard, B., Stander, N., Sulpizio, J. A., and Goldhaber-Gordon, D.: Phys. Rev. B **78**, 121402 (2008).

[50] Shytov, A. V., Rudner, M. S., and Levitov, L. S.: Phys. Rev. Lett. **101**, 156804 (2008).